Materials Today Physics 10 (2019) 100126

Contents lists available at ScienceDirect

Materials Today Physics

journal homepage: https://www.journals.elsevier.com/materials-today-physics

Determining phonon mean free path spectrum by ballistic phonon resistance within a nanoslot-patterned thin film

Q. Hao [*], Y. Xiao, Q. Chen

Department of Aerospace and Mechanical Engineering, University of Arizona Tucson, AZ, 85721-0119, USA

A R T I C L E   I N F O

Article history:
Received 5 May 2019
Received in revised form
21 June 2019
Accepted 10 July 2019
Available online 17 July 2019

Keywords:
Mean free path reconstruction
Thin film
Ballistic thermal resistance
Nanoslot

A B S T R A C T

At microscales to nanoscales, classical size effects in heat conduction play an important role in suppressing the thermal transport process. Such effects occur when the characteristic lengths become commensurate to the mean free paths (MFPs) of heat carriers that are mainly phonons for non-metallic crystals. Beyond existing experimental efforts on thin films using laser-induced thermal gratings, this work provides the theoretical analysis for a new approach to extract the effective phonon MFP distribution for the in-plane heat conduction within a thin film or flake-like sample. In this approach, nanoslots are patterned on a suspended thin film. Phonons will transport ballistically through the neck region between adjacent nanoslots if the phonon MFPs are much longer than the neck width. The associated 'ballistic thermal resistance' for varied neck dimensions can then be used to reconstruct the phonon MFP distribution within the film. The technique can be further extended to two-dimensional materials when the relaxation time approximation is reasonably accurate.

1. Introduction

One central topic of nanoscale heat transfer is to tailor the thermal properties of a material with the nanostructuring approach. When the structure size becomes comparable with or shorter than the bulk mean free path (MFP) Λ of some phonons, these phonons are forced to scatter more at boundaries or interfaces and the thermal transport can be strongly suppressed [1,2]. In principle, phonon MFPs in a bulk material usually have a wide distribution, ranging from nanometers to millimeters [3–5]. As one major input for phonon transport analysis, the employed phonon MFPs can largely affect the calculation results.

In simplified analysis, the gray-body approximation is applied to a bulk material, in which all phonons share the same phonon MFP and group velocity. Following this, an averaged Λ~43 nm is estimated for bulk Si using the kinetic relationship, $k_L = \frac{c v_g \Lambda}{3}$, where k_L, c, and v_g are the lattice thermal conductivity, volumetric phonon specific heat, and averaged phonon group velocity, respectively [6]. This is in contrast with thin-film measurements that suggest the dominant phonon MFP in Si to be ~300 nm at 300 K [7]. More recent first-principles calculations for energy-dependent Λ suggest that around 50% of the room temperature k_L is contributed by phonons with MFPs longer than 1 μm [5]. Correspondingly, a constant Λ~43 nm fails to explain the remarkable phonon size effects observed in microporous Si films [8], which can only be explained after considering Λ dependence on the phonon angular frequency ω and branch i [9].

Tremendous computational efforts have been dedicated to extracting the phonon MFP distribution. In the simplest approach, the temperature-dependent k_L of a bulk material can be fitted to determine the parameters used in the $\Lambda(\omega, i)$ expressions for different phonon scattering mechanisms [10]. Even for the same phonon scattering mechanism, however, different $\Lambda(\omega, i)$ expressions can be found in the literature. Large uncertainties exist because of employed $\Lambda(\omega, i)$ expressions and numerous fitting parameters. Without curve fittings, $\Lambda(\omega, i)$ can now be directly computed from first principles [5,11,12] and can be consistent with the phonon MFP spectrum obtained in pump probe measurements [13,14]. Beyond Si, first-principles computations of phonon MFPs have also been carried out on other materials with relatively simple atomic structures [3,4]. For complicated materials with a large number of atoms per primitive cell [15,16], such computations become very challenging because of the huge computational load. In this aspect, experimental techniques to extract the phonon MFP distribution in arbitrary materials is important not only for

---

* Corresponding author.
E-mail address: qinghao@email.arizona.edu (Q. Hao).

https://doi.org/10.1016/j.mtphys.2019.100126

validating computations but also for novel materials that are difficult to be studied by first-principles computations.

In experiments, the most successful technique to extract the phonon MFP spectrum is based on pump probe measurements [1]. These measurements use a probe laser to detect the temperature variation of the sample surface that is thermally excited by a pump laser. When the size D of the heating patterns is reduced, the lattice thermal conductivity contributed by a phonon with MFP $\Lambda(\omega, i) \gg D$ scales down, e.g. following $\frac{k_L(\omega,i)}{k_{L,Bulk}(\omega,i)} \sim \frac{D}{\Lambda(\omega,i)}$ [17]. The ballistic transport of these long MFP phonons leads to a ballistic thermal resistance (R_b) that is determined by D and $\Lambda(\omega, i)$. The adjusted D includes the thermal penetration depth by changing the modulation frequency [14,18,19], the laser beam diameter [20], the period of laser-induced thermal gratings on a suspended Si film [21,22], width of periodic metal lines [23,24], and the size of periodic laser-heated Al nanopillars [13]. Among these, the metallic patterns can cover a wide range of phonon MFPs, whereas other heating patterns cannot achieve sub-200 nm D values. As the most advanced method, a metal-polymer bilayer can be further coated in regions surrounding the Al pillars to prevent laser heating of the sample in these regions and minimize the contribution of these surrounding regions on the reflected probe-beam signal [13].

Despite the advancement of pump probe techniques, the employed metallic patterns may affect the lattice vibration modes within a suspended thin film [25,26], which should be avoided for the proposed phonon MFP studies. In recent experiments on Si nanobeams with periodic arrays of Al nanopillars, the reduced k of the nanobeams is also attributed to the surface roughness and the amorphous layer under the pillars [27]. In practice, however, phonon MFP distributions within a thin film are of their own importance when (1) single-crystal bulk samples cannot be easily synthesized (e.g. $Na_xCoO_{2-\delta}$ microflakes as the best p-type thermoelectric oxide [28]); (2) thin films are directly grown on a substrate and can be different from their bulk counterparts because of stress/strain and unintentional defects. Therefore, it is critical to extend the phonon MFP studies to thin films and still keep the capability of probing phonons with down to a few nanometer MFPs.

In this work, the theoretical analysis is provided for a different technique to experimentally extract the phonon MFP distribution, which is based on the in-plane thermal measurements of nanoslot-patterned thin films. A similar structure has been measured previously, but the focus is on the phonon transmission across a row of nanoslots between two adjacent suspended isothermal membranes [29]. In a simpler case, the bulk phonon MFP distribution has been extracted by measuring Si membranes with varied thicknesses [30]. Different from above studies, our proposed approach instead focuses on the ballistic resistance R_b introduced into a thin film, as the result of ballistic transport of long MFP phonons through the neck between patterned nanoslots. In this case, a row of nanoslots should be patterned in the middle of a film that is longer than majority phonon MFPs. By varying the neck width between adjacent nanoslots and thus R_b, the phonon MFP distribution within a thin film can be extracted. The phonon MFP distribution for the bulk counterpart can be further derived for special cases, i.e. completely diffusive film-surface phonon reflection at 300 K for a typical film-surface roughness [31].

In the literature, classical phonon size effects and sometimes phonon wave effects have been widely studied for Si thin films with periodic nanopores [32–38]. However, no studies have been carried out on the phonon MFP reconstruction, mainly because of the difficulty in obtaining a simple but accurate analytical model for the inverse phonon transport analysis. When k_L is computed by modifying the bulk phonon MFPs with a characteristic length or limiting dimension L_c of the nanoporous structure, different L_c expressions [39–44] have been proposed, but the predicted k_L for arbitrary nanoporous geometries can often diverge from those given by solving the phonon Boltzmann Transport equation (BTE) [9,45,46]. In addition, varied pore-edge defects and roughness across a real film can add more complexity to the data analysis [44,47–49]. In contrast, an accurate characteristic length L_c can be derived for nanoslot-patterned thin films and be directly used for phonon MFP reconstruction in this work. In nanofabrication, patterning a few nanoslots can also have better structure control than patterning numerous periodic nanopores, particularly when an ultrasmall L_c is required to probe the k_L contribution of short MFP phonons.

2. Extracting in-plane phonon MFP distributions with varied ballistic thermal resistances in film-like samples

2.1. Phonon Monte Carlo simulations for a nanoslot-patterned thin film

Fig. 1a shows the studied nanoslot-patterned thin film sandwiched between two thermal reservoirs, which is consistent with typical measurements using two isothermal membranes bridged by the measured thin film [35,36]. For potential thermoelectric applications, similar structures have also been introduced for graphene to reduce its intrinsically high thermal conductivity [50]. In this work, the structure-dependent thermal conductance of the film is used to extract the phonon MFP distribution from the inverse phonon transport analysis.

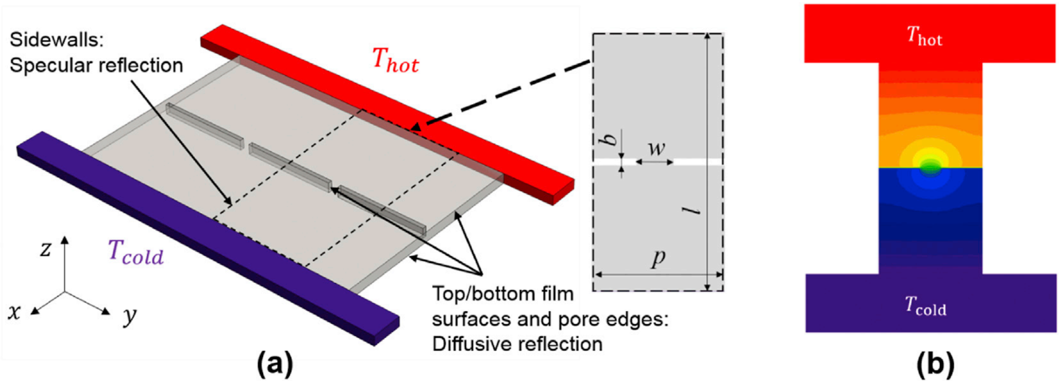

Fig. 1. (a) Illustration of a thin film with a row of periodic nanoslots pattered. The boundary conditions are indicated. As the top view, the nanoslot pitch p, film length l, neck width w, and depth b are shown in the inset. (b) A typical temperature profile for one period, as computed by frequency-dependent phonon MC simulations. A temperature jump may further occur at the film-reservoir junctions because of strongly ballistic phonon transport within a film.

In virtual experiments, frequency-dependent phonon Monte Carlo (MC) simulations are carried out to find the k_L of a given nanoslot-patterned thin film [46]. As one method to solve the phonon BTE, phonon MC simulations track the phonon transport and scattering to statistically obtain the BTE solution. To be consistent with aforementioned measurements, the computed thin film is sandwiched between two blackbodies with ΔT as the applied temperature difference [51,52]. The temperature profile for a typical 70-nm-thick nanoslot-patterned thin film with a 100 nm neck width is presented in Fig. 1b. For a single period, its left and right sidewalls are treated as specular because of structure symmetry. Other boundaries, such as the film top and bottom surfaces and typically rough nanoslot edges, are assumed to diffusively scatter phonons. This assumption is typically accurate at 300 K or above, where even ~1 nm surface roughness can lead to almost completely diffusive phonon scattering [31]. Experimental studies on the relationship between the surface roughness and the phonon specularity can be found elsewhere [53–55]. For ultrathin films, the emerging flexural modes should also be addressed for phonon transport [56]. These boundary conditions are marked in Fig. 1a, and the top view of one period is further shown in the inset.

One major problem for phonon MC simulations lies in its poor computational efficiency, which limits the early frequency-dependent phonon MC studies to nanosized structures [46]. This challenge has been recently solved by a new deviational phonon MC technique, which was developed by Péraud and Hadjiconstantinou [57]. Instead of tracking a huge number of phonons, this new technique only focuses on phonons related to the deviation of the phonon distribution function f from the equilibrium f_0 (i.e. Bose-Einstein distribution) at a reference temperature. This enables phonon MC simulations for the proposed microsized thin films.

2.2. *Phonon MFP extraction from the simulated thermal conductance of nanoslot-patterned films*

The phonon MFP distribution can be constructed by comparing the measured in-plane effective thermal conductivity k_{Rb} of a thin film with patterned nanoslots and that for a reference solid thin film (k_{Ref}). In real experiments, both the patterned film and the reference film can be measured to compare. Without considering the contribution of charge carriers to thermal transport, the thermal conductivity k is approximated as the lattice contribution k_L. For heavily doped samples, k_L can be obtained by subtracting the computed electronic contribution k_E, as demonstrated in numerous studies [58]. In this work, experimental results are replaced with simulated k_{Rb} and k_{Ref} to demonstrate the data analysis. A total number of M samples with varied neck width w can be measured, keeping other geometric parameters unchanged. For the ith ($i = 1, 2, 3, \cdots M$) measurements, the ratio $r_i = \frac{k_{Rb}}{k_{Ref}}$ is given as

$$r_i = \int_0^\infty S(\eta_i) f(\Lambda_{in}) \mathrm{d}\Lambda_{in} = \int_0^\infty K(\eta_i) q_i F(\Lambda_{in}) \mathrm{d}\Lambda_{in}\,, \tag{1}$$

in which Λ_{in} is the effective in-plane phonon MFP within a solid thin film, $\eta = \frac{\Lambda_{in}}{w}$, the Kernel function $K(\eta) = -dS/d\eta$, $q = \frac{d\eta}{d\Lambda_{in}} = \frac{1}{w}$, and $F(\Lambda_{in}) = \int_0^{\Lambda_{in}} f(\Lambda_{in}^{'}) \mathrm{d}\Lambda_{in}^{'}$ is the accumulated phonon MFP distribution. The suppression function S describes the in-plane heat flow reduction because of fabricated nanoslots. Integration by parts is used in the above conversion from $f(\Lambda_{in})$ to $F(\Lambda_{in})$, which also assumes $F(0) = 0$, $F(\infty) = 1$, and $S_i(\infty) = 0$. Here, Λ_{in} is modified from the bulk phonon MFP Λ_{Bulk} based on the film thickness t and probability of specular phonon reflection (i.e. specularity) on film boundaries, known as the Fuchs-Sondheimer model [31]. Assuming completely diffusive film-surface phonon scattering, the effective in-plane phonon MFP Λ_{in} inside a solid film without nanoslot patterns is given as

$$\frac{\Lambda_{in}}{\Lambda_{Bulk}} = 1 - \frac{3\Lambda_{Bulk}}{2t} \int_0^1 \left(x - x^3\right) \left[1 - \exp\left(-\frac{t}{\Lambda_{Bulk}} \frac{1}{x}\right)\right] \mathrm{d}x. \tag{2}$$

Mathematically, the integral in Eq. (1) can be seen as an ill-posted problem which could have infinite solutions. However, a unique solution of Eq. (1) can still be obtained without knowing the phonon transport information inside the structure [59]. In numerical integration, $F(\Lambda_{in})$ at N discretized Λ_{in} nodes is selected. Equation (1) is changed into

$$r_i = \sum_{j=1}^{N} K(q_i \Lambda_{in,j}) q_i F(\Lambda_{in,j}) \beta_j = \sum_{j=1}^{N} A_{i,j} F(\Lambda_{in,j}), \tag{3}$$

where β_j is the quadrature weight for each node, $q_i = \frac{1}{w_i}$ for the ith sample, $A_{i,j} = K(q_i \Lambda_{in,j}) q_i \beta_j$ is a $M \times N$ matrix. Here trapezoidal rule is used to determine quadrature points and weights.

With the measurement data of M samples, the discretized MFP distribution $F(\Lambda_{in,j})$ can be determined by solving Eq. (1) as an ill-posed problem. There are various approaches to solve such problems, including the popular Tikhonov regularization [60], Lasso regression [61], and Lanczos Bidiagonalization [62]. This work adopts the Tikhonov regularization to minimize a penalty function P:

$$P = \left\| AF - \frac{k_{Rb}}{k_{Ref}} \right\|_2^2 + \alpha \left\| \Delta^2 F \right\|_2^2. \tag{4}$$

In Eq. (4), $\Delta^2 F = F_{j+1} - 2F_j + F_{j-1}$ and $\| \cdot \|_2^2$ is the square of the second-norm. k_{Rb} and k_{Ref} represent the measured thermal conductance of the nanoslot-patterned thin film and solid thin film, respectively. In addition, α represents a regularization parameter to balance the accuracy penalty as the 1st term on the right hand side of Eq. (4) and the smoothness penalty as the 2nd term on the right hand side of Eq. (4). Some restrictions are imposed to this convex optimization: The accumulated phonon MFP distribution F should be smooth and increase monotonically from $F(0) = 0$ to $F(\infty) = 1$. Detailed discussions of the convex optimization can be found in other studies [13,24,63–65], in which a MATLAB-based package CVX was used for this purpose [24,59].

2.3. *Suppression function* **S** *predicted by phonon MC simulations and an analytical model*

One major task of the theoretical analysis is to obtain the employed η-dependent suppression function S. As one approach, $S(\eta)$ can be derived from the phonon BTE for some geometries [66,67]. For completely ballistic phonon transport through an aperture such as the neck between nanoslots, simpler analytical models can be found [50,68]. Beyond these studies, a general $S(\eta)$ expression from the ballistic to diffusive transport regimes is derived here and employed for the following phonon MFP reconstruction.

In the analytical modeling, the computed Λ_{in} already incorporates the possible diffusive phonon scattering by the top and bottom film surfaces. In this case, a solid thin film with rough top and bottom surfaces is converted into a solid thin film with smooth surfaces but a phonon MFP Λ_{in} reduced from Λ_{Bulk}. The nanoslot patterns further modify Λ_{in} within the x-y plane. To extract $S(\eta)$ in Eq. (1), the diffusive film-surface phonon scattering should not be double counted so that specular phonon reflection is enforced for the top and bottom surfaces of the film [51]. On the other hand, rough nanoslot edges caused by nanofabrication should diffusively reflect phonons. For any given constant phonon MFP Λ_{in}^* and thus a constant $\eta = \frac{\Lambda_{in}^*}{w}$ for one given w value, frequency-independent phonon MC simulations are used here to predict k_{R_b} for this given Λ_{in}^*. The reference k_{Ref} can be easily computed with Λ_{in}^*, leading to $S(\eta) = \frac{k_{Rb}}{k_{Ref}}$ for a particular set of Λ_{in}^* and w values. The computed $S(\eta)$ is shown in Fig. 2a as crosses. The considered structure is a 1-μm long film ($l = 1$ μm) with smooth film surfaces as the quasi-2D case. The neck width w varies from 5 nm to 350 nm, with constant $b = 5$ nm and $p = 500$ nm. In above calculations, Λ_{in}^* is not the averaged in-plane phonon MFP within a film but a variable that scans over the whole Λ_{in} range to find the complete $S(\eta)$ curve. The obtained $S(\eta)$ can be directly used for frequency-dependent phonon transport analysis such as Eq. (1). Similar approaches can be found in the literature. The modification of a particular phonon MFP within nanostructures can be directly extracted with a MC technique based on ray-tracing or path sampling [37,69–72] or solving a MFP-dependent phonon BTE [73,74]. This procedure can be repeated for varied phonon MFPs. The modified phonon MFPs across the whole MFP spectrum can then be used for k_L calculations considering frequency-dependent phonon MFPs.

Because frequency-independent phonon MC simulations can be time-consuming to acquire the cross symbols in Fig. 2a, an analytical model is also developed to estimate $S(\eta)$ as the lines in Fig. 2a. First, the in-plane Λ_{in} is modified by a characteristic length L_c associated with the two-dimensional patterns such as nanoslots and finite film length:

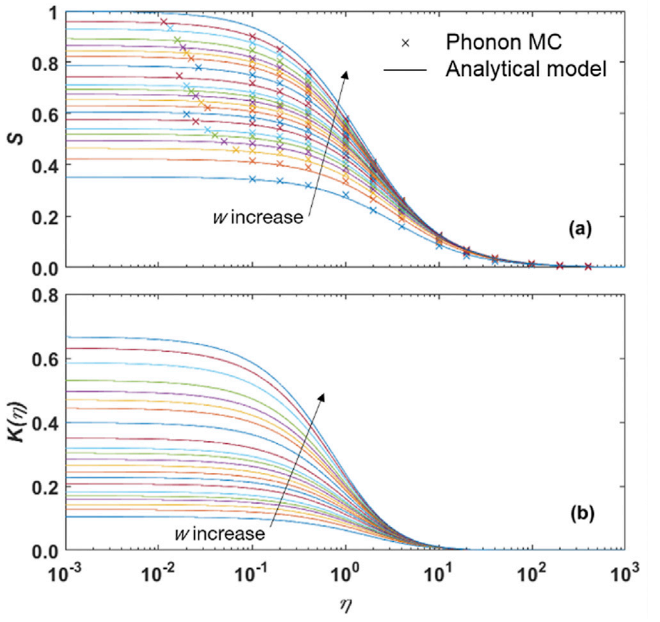

Fig. 2. (a) Suppression function $S(\eta)$ Using Eq. (6) for quasi-2D cases. From the bottom to top curves, $w = 5, 10, 15, 20, 25, 30, 40, 50, 60, 70, 80, 90, 100, 120, 150, 180, 200, 220, 250, 300, 350$, and 500 nm, respectively. Symbols are from phonon MC simulations assuming a constant phonon MFP. Symbols and curves have the same color for w up to 350 nm. (b) Kernel function $K(\eta)$ using fitted L_c values for $w = 5$–350 nm and $L_c = \frac{3l}{4}$ for $w = 500$ nm. Along the arrow direction, w values match those in (a). MFP, mean free path; MC, Monte Carlo. (For interpretation of the references to color in this figure legend, the reader is referred to the Web version of this article.)

$$\frac{1}{\Lambda_{eff}} = \frac{1}{\Lambda_{in}} + \frac{1}{L_c}. \tag{5}$$

In this case, the effective lattice thermal conductivity is calculated based on the kinetic relationship $k_L = \frac{cv_g\Lambda_{eff}}{3}$ [31], with the phonon specific heat c and group velocity v_g unchanged from bulk materials. For frequency-dependent analysis, k_L is integrated over the whole phonon spectrum and summed up over different phonon branches. Then k_{Rb} is computed as $k_{Rb} = kH_w \approx k_L H_w$, where H_w is the correction factor to account for the reduced heat transfer in cross-sectional area because of nanoslots. This correction factor H_w can be computed using the Fourier's law by comparing the thermal conductance of a nanoslot-patterned thin film and that of a solid thin film. In this work, the thermal conductance calculation is performed using COMSOL Multiphysics software package. Additional classical phonon size effects only reduce the solid-counterpart k_L that is based on modified phonon MFPs in Eq. (5). The combination of the Fourier's law prediction and k_L reduction because of modified phonon MFPs has been found to be an accurate way to predict the thermal conductivities of periodic nanoporous Si films [9,45,72] and nanocomposites [75,76].

For the reference solid film, k_{Ref} has Λ_{in} as the phonon MFP in the kinetic relationship. By comparing k_{Ref} and k_{Rb}, an analytical model of the suppression function S can be derived as

$$S(\eta) = \frac{\left(\frac{1}{\Lambda_{in}} + \frac{1}{L_C}\right)^{-1}}{\Lambda_{in}} H_w = \frac{L_c}{\Lambda_{in+}L_c} H_w = \frac{L_c}{\eta w + L_c} H_w. \tag{6}$$

When Λ_{in} approaches zero and leads to completely diffusive phonon transport, the Fourier's law is invoked so that $S(\eta = 0) = H_w$. At the limit $\Lambda_{in} \to \infty$, $S(\infty) = 0$ is obtained. With H_w known for each w values, one way to determine the corresponding characteristic length L_c is to use Eq. (6) to fit the special frequency-independent phonon MC simulation results, as curves in Fig. 2a. For $\eta < 0.01$, $S(\eta)$ saturates at H_w, i.e. the intersection between the $S(\eta)$ curve and the x-axis. With fitted L_c, the Kernel function $K(\eta)$ can be acquired analytically (Fig. 2b). As an extreme case with $w = p = 500$ nm and thus no nanoslots, $L_c = \frac{3l}{4}$ is directly used to compute $S(\eta)$ for a solid film, [77] and fitting with frequency-independent phonon MC simulations is unnecessary.

Alternatively, L_c can also be derived by examining the thermal conductance of the nanoslot-patterned thin film at the limit $\Lambda_{in} \to \infty$. At this limit, the neck between two adjacent nanoslots functions as an aperture for the phonon transport. In this situation, the neck receives black-body emission from the thermal reservoirs at both ends of the structure (Fig. 1a). Following a similar derivation as in previous studies [68], the associated thermal conductance G_{Rb} for one period is:

$$G_{Rb} = \frac{wt}{4} \sum_{i=1}^{3} \int_0^{\omega_{max,i}} C_i(\omega) v_{g,i}(\omega) d\omega, \tag{7}$$

where the product wt stands for the cross-section area of the neck. The phonon branch and angular frequency are denoted as i and ω, respectively. This G_{Rb} is derived as the net heat flow across a neck divided by the temperature difference applied across the whole structure. More associated analysis can be found elsewhere [50,78]. Along another line, Eq. (5) suggests $\Lambda_{eff} = L_c$ at $\Lambda_{in} \to \infty$ so that

$$G_{Rb}=\frac{kH_wpt}{l}=\frac{H_wpt}{l}\frac{1}{3}\sum_{i=1}^{3}\int_{0}^{\omega_{max,i}}C_i(\omega)v_{g,i}(\omega)L_c d\omega. \tag{8}$$

Exact matching between Eqs. (7) and (8) for the spectral contribution of each phonon mode yields an analytical expression of L_c:

$$L_c=\frac{w}{p}\frac{3l}{4H_w}, \tag{9}$$

which can also be used in Eq. (6) for $S(\eta)$ predictions. In Eq. (9), the structure simply becomes a solid film at $w = p$. In this extreme case, the correction factor $H_w = 1$ and the corresponding $L_c = \frac{3l}{4}$ in Eq. (9). This L_c value also matches that proposed for a solid film in an early study [77]. Fig. 3 shows the comparison between L_c fitted from the MC-simulated $S(\eta)$ curves (squares) and L_c computed with Eq. (9) (solid line). The divergence is within 5% for most w values. To probe the contribution of phonons with down to ~10 nm MFPs, here L_c is down to 16.9 nm for the smallest $w = 5$ nm. Despite a reasonably good agreement between the fitted and derived L_c values, particular attention should be paid to the fitted L_c value at $w < 10$ nm (Solid line in Fig. 3 inset), which becomes smaller than predictions by Eq. (9). This is because of an additional conduction thermal resistance $R_{neck} = \frac{b}{wtk_{neck}}$ added by the neck region with depth b, where k_{neck} is the effective thermal conductivity for the neck region with diffusive phonon boundary scattering on its sidewalls. By reducing b to zero or setting specular phonon reflection for the neck sidewalls, the divergence between the fitted and predicted L_c values can be eliminated.

To further investigate the influence of b on L_c, nanoslot-patterned structures with fixed w, l, p but varied b are simulated. As discussed earlier, the diffusive phonon scattering by the top and bottom film surfaces should not be double counted in L_c. In this situation, specular phonon reflection is again enforced on the top and bottom surfaces to derive corrected L_c values. In principle, the neck region is in analogy to a thin film with its film thickness as the neck width w here. Assuming completely diffusive film-surface phonon scattering as that for the neck sidewalls, Eq. (2) can be used to modify Λ_{in} and obtain the effective phonon MFP Λ_{neck} within the neck region, yielding k_{neck} and R_{neck}. For the whole film, this R_{neck} is added to the predicted $1/G_{Rb}$ for a nanoslot-patterned film with the neck depth $b \rightarrow 0$. The solid lines in Fig. 4 present the predicted total thermal resistance R_{total} of different nanoslot-patterned films with a fixed thickness of 10 nm. Specular phonon reflection is assumed on the top and bottom surfaces of these structures. The possible change of the phonon dispersion and phonon scattering rates within the neck region is neglected here but can be included in more accurate analysis, as shown in phonon studies of nanowires [79–81]. The prediction agrees well with phonon MC simulations considering frequency-dependent phonon MFPs given by first-principles calculations [5] (symbols in Fig. 4). In practice, b should be minimized in nanofabrication. Compared with ballistic thermal resistance R_b, R_{neck} is thus negligible, and Eq. (9) can be used to accurately determine L_c. When b is relatively large, Eq. (7) becomes

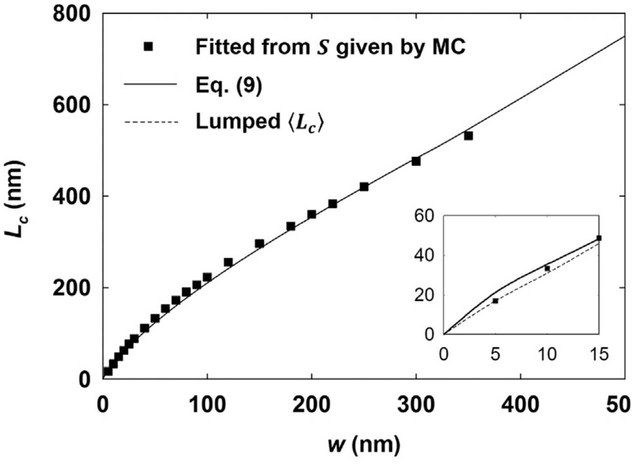

Fig. 3. Comparison between L_c fitted from $S(\eta)$ curves given by frequency-independent phonon MC simulations (squares) and L_c computed with Eq. (9) (solid line) or the lumped L_c (dashed line). MC, Monte Carlo.

$$\begin{aligned}\frac{1}{G_{total}}&=\sum_{i=1}^{3}\int_{0}^{\omega_{max,i}}\left[\frac{4}{C_i(\omega)v_{g,i}(\omega)wt}+\frac{b}{wtk_{neck}}\right]d\omega\\&=\sum_{i=1}^{3}\int_{0}^{\omega_{max,i}}\frac{4+\frac{3b}{\Lambda_{neck,i}(\omega)}}{C_i(\omega)v_{g,i}(\omega)wt}d\omega.\end{aligned} \tag{10}$$

Comparing Eq. (10) with Eq. (8) for the spectral contribution from individual phonon modes yields

$$L_c=\frac{w}{p}\frac{3l}{\left(4+3b/\Lambda_{neck,i}(\omega)\right)H_w}, \tag{11}$$

where L_c varies with different Λ_{neck} values and is no longer a constant as L_c in Eq. (9). To simplify, a lumped L_c averaged over all phonon modes can be used and is expressed as

$$L_c=\frac{3l}{H_wpt}G_{total}\Big/\sum_{i=1}^{3}\int_{0}^{\omega_{max,i}}C_i(\omega)v_{g,i}(\omega)d\omega. \tag{12}$$

This lumped L_c is plotted in the inset of Fig. 3 as a dashed line and shows better agreement with the L_c values fitted from $S(\eta)$ curves given by frequency-independent phonon MC simulations.

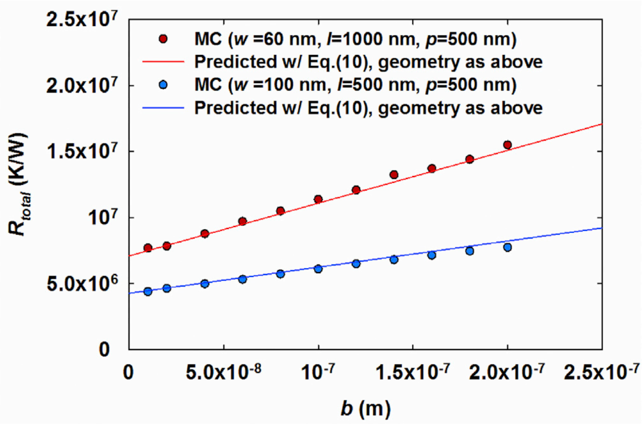

Fig. 4. Comparison between the R_{total} given by frequency-dependent phonon MC simulations and R_{total} predicted by Eq. (10). MC, Monte Carlo.

3. Results and discussion

3.1. Temperature profiles within nanoslot-patterned Si films sandwiched between two blackbodies

As virtual experiments, the room-temperature k_{Rb} and thus k_{Rb}/k_{Ref} ratios are first computed by frequency-dependent phonon MC simulations for the proposed thin film with varied neck width w between nanoslots. Without losing the generality, the first-principles phonon MFPs for bulk Si [5], as validated by experiments [13], are used in phonon MC simulations. In phonon MC simulations, a film thickness t of 70 nm is assumed, with rough film surfaces for completely diffusive phonon reflection. Other geometry parameters are consistent with those used in Fig. 2, i.e. $l = 1$ μm, $b = 5$ nm, and $p = 500$ nm.

Figs. 5a–d shows the temperature contours of representative nanoslot-patterned thin films with two ends in contact with blackbody heat reservoirs fixed as 305 K and 295 K, respectively. For small w values, particular attention should be paid to the long time required for the phonon MC code to converge. In principle, the chance for a phonon to pass the neck regions becomes very small with a decreased w/p ratio. Therefore, a longer simulation time is needed to statistically obtain the impact of the neck region on the thermal conductivity of the whole film. Fig. 5e further presents the heat-flow-direction temperature profiles along the symmetric line of a period.

3.2. Reconstructed phonon MFP distribution

The k_{Rb}/k_{Ref} ratios given by frequency-dependent phonon MC simulations are shown as a function of w in Fig. 6a. The frequency-dependent phonon MFPs calculated by first principles for bulk Si [5] are used in phonon MC simulations. The values of w match those in Fig. 2. As anticipated, the k_{Rb}/k_{Ref} ratio monotonously increases as w is expanded to the pitch p. However, this ratio cannot reach 100% at $w = p$ because of the phonon MFP constriction by the finite film length l, where $3l/4$ should be used to modify the bulk phonon MFP in k_L predictions [77]. Following the description in Section 2.2, $F(\Lambda_{in})$ can be reconstructed through convex optimization. The fitted L_c is used to take the depth b influence into consideration. Here, $M = 21$ samples and $N = 200$ logarithmic-spaced discretized intervals are used in the MFP reconstruction. The obtained MFP distribution function F is found to be less sensitive to the smooth factor α in the range of $0.5 < \alpha < 2.0$, as indicated by the colored band in Fig. 6b. A smooth factor $\alpha = 1.0$ is adopted. The reconstructed $F(\Lambda_{in})$ generally agrees with the employed first-principles $F(\Lambda_{in})$. Some divergence is anticipated because the reconstructed $F(\Lambda_{in})$ is a smooth curve, in contrast with the irregular first-principles $F(\Lambda_{in})$ curve. For different α values, however, the reconstructed F always matches well with employed first-principles F at $F \approx 60\%$. At the smallest $w = 5$ nm, the characteristic length is $L_c = 16.9$ nm, which could limit the accuracy of the phonon MFP reconstruction in the sub-10 nm regime. To check this, the same inverse phonon transport studies are carried out after adding one more k_{Rb}/k_{Ref} value at $w = 1$ nm, with the corresponding characteristic length reduced to $L_c = 5.0$ nm. Repeating the same procedure with $\alpha = 1.0$, the newly reconstructed $F(\Lambda_{in})$ is almost identical to $F(\Lambda_{in})$ using a minimum $w = 5.0$ nm, as shown in Fig. 6c. This negligible difference is also because of the relatively weak thermal conductivity contribution by phonons with sub-10 nm MFPs. Some divergence is anticipated when these ultra-short-MFP phonons become important to heat conduction, e.g. samples with significantly reduced phonon MFPs at high temperatures.

In Figs. 6b–c, at least 21 data points are used to ensure an accurate phonon MFP reconstruction. In practice, this can be very demanding for experiments. In fact, a reduced number of samples can also provide a reasonably good MFP reconstruction, as long as the corresponding L_c values cover the main phonon MFP range. To check this, Fig. 6d compares the reconstructed MFP distributions using 21, 11, and six samples. For 11 samples, the data points taken from Fig. 6a corresponds to $w = 5$, 15, 25, 40, 60, 80, 100, 150, 200, 250, and 350 nm. For six samples, the selected w values are 5, 50, 100, 150, 250, and 350 nm. The phonon MFP reconstruction with only six samples has a trivial deviation from that using 21 samples.

3.3. Tuning the characteristic length to better probe short-MFP phonons

To better sense ultra-short phonon MFPs, a smaller minimum L_c is required. According to Eq. (9), L_c is not only restricted by w but also related to l and p. Fig. 7a and b presents the variation of H_w and L_c with respect to w and l, respectively. Here $p = 500$ nm and $b = 1$ nm are fixed. In Fig. 7a, it can be observed that H_w becomes larger as l increases, which is because of the increased importance for the length-direction thermal resistance added to the ballistic thermal resistance R_b. Fig. 7b presents the L_c distribution with respect to w and l, where L_c has a stronger dependence on w. The lowest $L_c = 10.2$ nm is found at the minimum $w = 5$ nm and $l = 100$ nm. In nanofabrication, $w<5$ nm cannot be easily achieved with the standard electron beam lithography and dry etching. For suspended 2D materials, however, such a small neck region can be directly patterned with electron beam drilling [82].

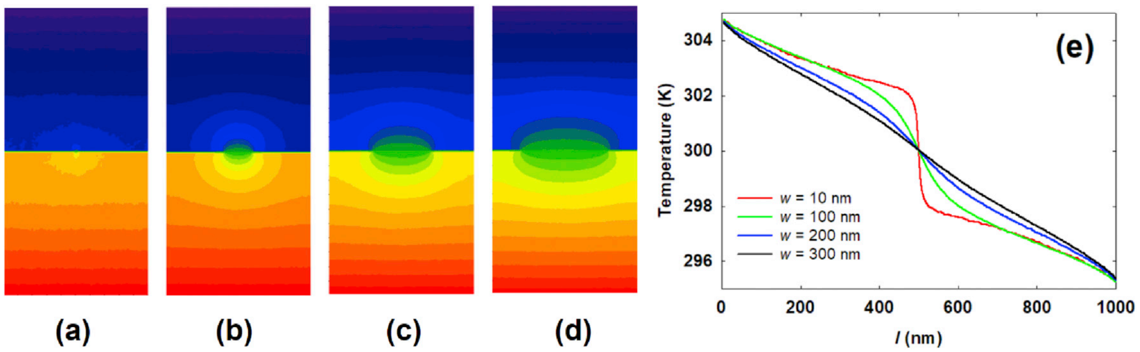

Fig. 5. Temperature contours of a nanoslot-patterned thin film with $l = 1$ μm, $b = 5$ nm, $p = 500$ nm. The neck width w is (a) 10 nm, (b) 100 nm, (c) 200 nm, and (d) 300 nm, respectively. (e) Temperature profiles along the central symmetric line of a period in (a) to (d).

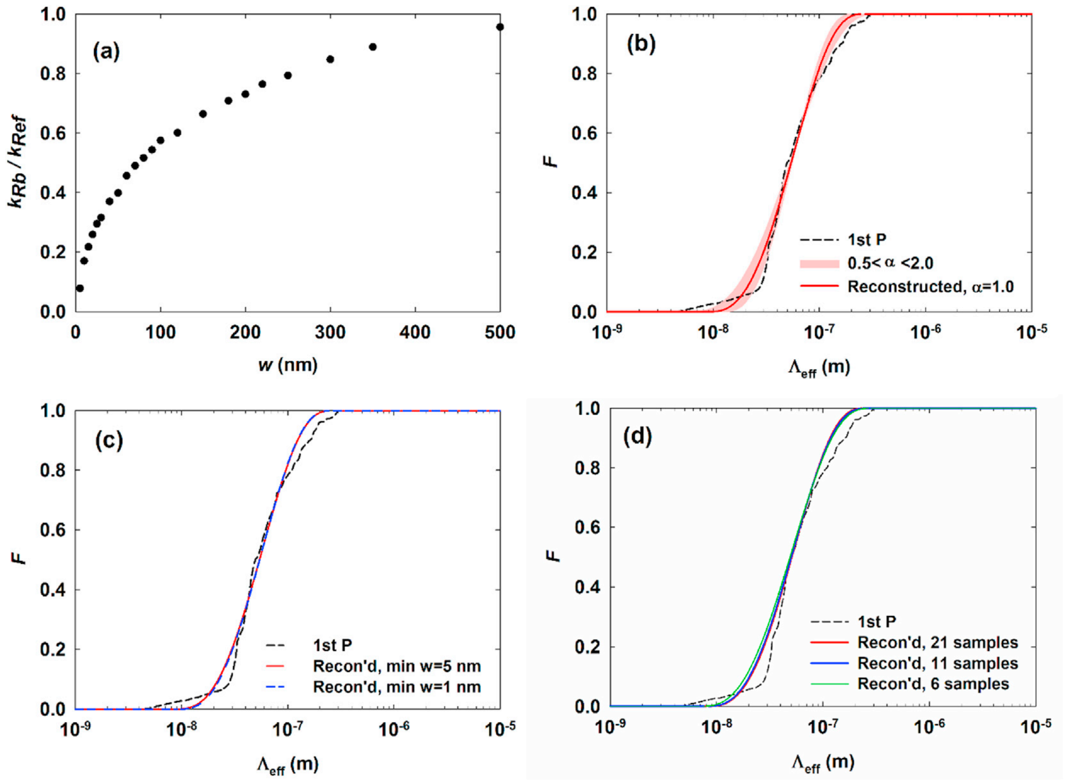

Fig. 6. (a) k_{Rb}/k_{Ref} ratio computed with first-principles bulk Si phonon MFPs in frequency-dependent phonon MC simulations. (b) Comparison between reconstructed MFP distribution $F(\Lambda_{in})$ and the employed first-principles $F(\Lambda_{in})$. (c) Three-way comparison between the employed fist-principles $F(\Lambda_{in})$, reconstructed MFP distributions with a minimum $w = 5$ nm or $w = 1$ nm. (d) Comparison between reconstructed MFP distribution using 21, 11, and six samples, where w varies from 5 nm to 350 nm in all three cases. MFP, mean free path; MC, Monte Carlo.

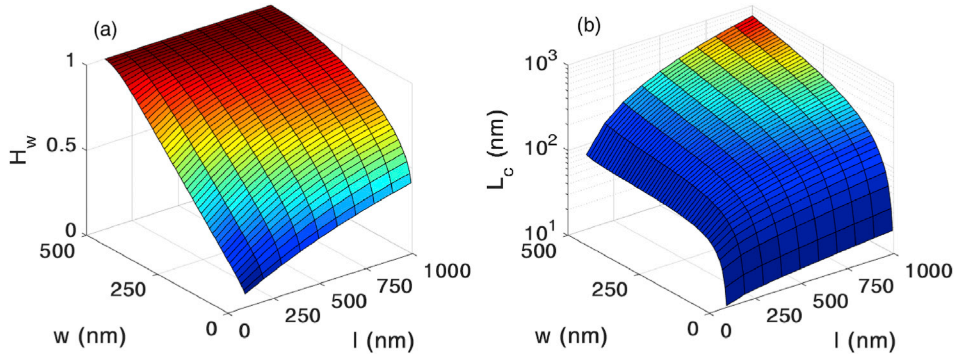

Fig. 7. The dependence of (a) reduction factor H_w and (b) L_c on w and l. Other dimensions are fixed at $p = 500$ nm and $b = 1$ nm.

3.4. Comparison between periodic nanoslot and nanopore patterns

The proposed nanoslot-patterned thin films form an interesting comparison with widely studied periodic nanoporous Si films [32–38]. It is now acknowledged that coherent phonon transport is only critical at low temperatures, where the dominant phonon wavelength scales up with $1/T$ and becomes comparable to the structure sizes. By comparing the thermal conductivities of periodic and aperiodic nanoporous film, wave effects because of coherent phonon interference was identified below 14 K for Si films with p>100 nm [37] or below 10 K for $p = 300$ nm [32]. In most cases, incoherent phonon transport is dominant for the thermal conductivity reduction, which is similar to nanoslot-patterned thin films.

For the phonon MFP reconstruction, one major problem for using such periodic nanoporous films is the lack of an accurate analytical model based on the phonon MFP modification using an effective characteristic length L_c. In principles, using the Matthiessen's rule in Eq. (5) to combine boundary phonon scattering and internal phonon scattering within a volume is not accurate [31]. For aligned nanopores with a pitch p and pore diameter d, MC ray tracing suggests $L_c = (4p^2 - \pi d^2)/\pi d$ as the geometric mean beam length for the structure [9,83]. This L_c is accurate when ballistic phonon transport is dominant in the structure. However, it is less accurate with increased internal phonon scattering and some modifications of L_c should be taken [9,45]. In the literature, the proposed characteristic lengths also include $L_c = \sqrt{p^2 - \pi d^2/4}$ as the square root of the solid area within a period [42], $L_c = p - d$ as the neck width [40,41], $L_c \sim 4p^2/\pi d$ as the reciprocal of the surface-to-volume ratio [39]. None of these L_c values are consistently accurate for arbitrary pitch-diameter combinations [9,45]. Clearly, $L_c = \sqrt{p^2 - \pi d^2/4}$ and $L_c = p - d$ are only valid for dense nanopores because $L_c > p$ is anticipated for sparse nanopores patterned across a film. In general, a consistent L_c cannot be expected for Eq. (5) over the whole phonon MFP spectrum, and the L_c expressions should be modified with a fitted geometrical factor to match the predictions by the phonon BTE [45]. The lack of an accurate analytical model for the predictions of the suppression function $S(\eta)$ and the kernel function $K(\eta)$ can largely increase the difficult level of the inverse phonon transport analysis. In practice, $S(\eta)$ and $K(\eta)$ can be obtained with a MC technique based on ray-tracing or path sampling [37,69,70] or by solving the MFP-dependent phonon BTE [73]. However, these techniques are very complicated and cannot be used to predict the whole $S(\eta)$ and $K(\eta)$ curves in an effective way. For a nanoslot-patterned thin film, phonons are mainly affected by the ballistic thermal resistance introduced by the neck width w. The structure complexity is largely reduced from that for periodic nanoporous Si films with varied pitches and pore diameters. The predicted characteristic length L_c does not need any modification by a geometric factor here.

Within periodic nanoporous films, the shape variation of individual nanofabricated pores across the whole film can add large uncertainties to the data analysis, along with varied pore-edge defects or roughness to affect the effective pore diameter and thus the neck width [44,47–49]. This makes such periodic nanoporous Si films unsuitable for the study of the phonon MFP distribution. For a thin films with only a few nanoslots, above uncertainties can be largely minimized in the data analysis using an averaged w revealed by the electron microscopy. The effective w value for each neck can be slightly expanded because of the amorphous pore edges, as suggested for nanoporous Si films in electron microscopy studies [35,47,48].

4. Conclusions

In summary, a new approach to determine the phonon MFP distribution $F(\Lambda_{eff})$ for the in-plane heat conduction in thin films is proposed in this work. An analytical solution for the suppression function S of nanoslot-patterned thin films is also proposed and can be employed to compute the transport properties of 2D materials using such patterns, such as nanoslot-patterned graphene [50] or MoS_2. For thin films and 2D materials, their in-plane phonon MFP distribution can be obtained with the proposed approach, whereas the widely used pump probe measurements can be largely restricted for suspended structures. Although the relaxation time approximation is found to be less accurate for 2D materials because of the importance of normal processes [84], such phonon MFP reconstructions can still yield the range of phonons MFPs [85] to be compared with existing calculations [86].

Beyond phonon MFP reconstructions, the proposed nanoslot patterns can also be used to enhance the thermoelectric performance of general thin films, in addition to the widely studied periodic nanoporous patterns [32–38]. When the characteristic length L_c is shorter than majority phonon MFPs but still longer than the dominant electron MFPs, the thermal conductivity can be dramatically reduced, but the electrical properties can still be maintained, leading to improved thermoelectric performance. In the analysis based on the BTE, the proposed L_c expression can be directly used to modify the electron and phonon MFPs to compute the thermoelectric properties.

Acknowledgments

The authors acknowledge the support from the U.S. Air Force Office of Scientific Research (award number FA9550-16-1-0025) for studies on nanoporous materials and National Science Foundation (grant number CBET-1651840) for phonon simulations. An allocation of computer time from the UA Research Computing High Performance Computing (HPC) and High Throughput Computing (HTC) at the University of Arizona is gratefully acknowledged. The authors would also like to thank Prof. Austin Minnich and Dr. Emigdio Chávez-Ángel for the valuable insights on convex optimizations and Dr. Hongbo Zhao for the help on phonon MC simulations.

References

[1] D.G. Cahill, P.V. Braun, G. Chen, D.R. Clarke, S. Fan, K.E. Goodson, P. Keblinski, W.P. King, G.D. Mahan, A. Majumdar, H.J. Maris, S.R. Phillpot, E. Pop, L. Shi, Appl. Phys. Rev. 1 (1) (2014): 011305.
[2] D.G. Cahill, W.K. Ford, K.E. Goodson, G.D. Mahan, A. Majumdar, H.J. Maris, R. Merlin, S.R. Phillpot, J. Appl. Phys. 93 (2) (2003) 793–818.
[3] T. Luo, G. Chen, Phys. Chem. Chem. Phys. 15 (10) (2013) 3389–3412.
[4] T. Feng, X. Ruan, J. Nanomater. 2014 (2014) 206370, 2014.
[5] K. Esfarjani, G. Chen, H.T. Stokes, Phys. Rev. B 84 (8) (2011): 085204.
[6] J.S. Blakemore, Solid State Physics, 2 ed., Cambridge University Press, Cambridge, 1985.
[7] Y. Ju, K. Goodson, Appl. Phys. Lett. 74 (20) (1999) 3005–3007.
[8] D. Song, G. Chen, Appl. Phys. Lett. 84 (5) (2004) 687–689.
[9] Q. Hao, Y. Xiao, H. Zhao, J. Appl. Phys. 120 (6) (2016): 065101.
[10] C. Dames, G. Chen, in: D.M. Rowe (Ed.), Thermoelectrics Handbook: Macro to Nano vol. 42, CRC Press, Boca Raton, FL, USA, 2005, 41-16.
[11] A. Ward, D. Broido, Phys. Rev. B 81 (8) (2010): 085205.
[12] D.A. Broido, M. Malorny, G. Birner, N. Mingo, D.A. Stewart, Appl. Phys. Lett. 91 (23) (2007) 231922–231923.
[13] Y. Hu, L. Zeng, A.J. Minnich, M.S. Dresselhaus, G. Chen, Nat. Nanotechnol. 10 (8) (2015) 701–706.
[14] K.T. Regner, D.P. Sellan, Z. Su, C.H. Amon, A.J. McGaughey, J.A. Malen, Nat. Commun. 4 (2013) 1640.
[15] E.S. Toberer, A. Zevalkink, G.J. Snyder, J. Mater. Chem. 21 (40) (2011) 15843–15852.
[16] Q. Hao, D. Xu, N. Lu, H. Zhao, Phys. Rev. B 93 (20) (2016) 205206.
[17] G. Chen, J. Heat Transf. 118 (3) (1996) 539–545.
[18] Y.K. Koh, D.G. Cahill, Phys. Rev. B 76 (7) (2007): 075207.
[19] J.P. Freedman, J.H. Leach, E.A. Preble, Z. Sitar, R.F. Davis, J.A. Malen, Sci. Rep. 3 (2013) 2963.
[20] A.J. Minnich, J. Johnson, A. Schmidt, K. Esfarjani, M. Dresselhaus, K.A. Nelson, G. Chen, Phys. Rev. Lett. 107 (9) (2011): 095901.
[21] J.A. Johnson, A.A. Maznev, M.T. Bulsara, E.A. Fitzgerald, T. Harman, S. Calawa, C. Vineis, G. Turner, K.A. Nelson, J. Appl. Phys. 111 (2) (2012): 023503.
[22] J.A. Johnson, A. Maznev, J. Cuffe, J.K. Eliason, A.J. Minnich, T. Kehoe, C.M.S. Torres, G. Chen, K.A. Nelson, Phys. Rev. Lett. 110 (2) (2013): 025901.
[23] M.E. Siemens, Q. Li, R. Yang, K.A. Nelson, E.H. Anderson, M.M. Murnane, H.C. Kapteyn, Nat. Mater. 9 (1) (2010) 26–30.
[24] L. Zeng, K.C. Collins, Y. Hu, M.N. Luckyanova, A.A. Maznev, S. Huberman, V. Chiloyan, J. Zhou, X. Huang, K.A. Nelson, Sci. Rep. 5 (2015) 17131.
[25] B.L. Davis, M.I. Hussein, Phys. Rev. Lett. 112 (5) (2014): 055505.
[26] R. Anufriev, M. Nomura, Phys. Rev. B 95 (15) (2017) 155432.
[27] R. Anufriev, R. Yanagisawa, M. Nomura, Nanoscale 9 (39) (2017) 15083–15088.
[28] F. Kenjiro, M. Tadashi, N. Kazuo, Jpn. J. Appl. Phys. 40 (7R) (2001) 4644.
[29] J. H. Seol, Ph.D. Dissertation, University of Texas at Austin, 2009..
[30] J. Cuffe, J.K. Eliason, A.A. Maznev, K.C. Collins, J.A. Johnson, A. Shchepetov, M. Prunnila, J. Ahopelto, C.M. Sotomayor Torres, G. Chen, K.A. Nelson, Phys. Rev. B 91 (24) (2015) 245423.
[31] G. Chen, Nanoscale Energy Transport and Conversion: A Parallel Treatment of Electrons, Molecules, Phonons, and Photons, Oxford University Press, New York, 2005.
[32] J. Maire, R. Anufriev, R. Yanagisawa, A. Ramiere, S. Volz, M. Nomura, Science advances 3 (8) (2017): e1700027.
[33] M. Nomura, J. Shiomi, T. Shiga, R. Anufriev, Jpn. J. Appl. Phys. 57 (8) (2018): 080101.
[34] M. Verdier, R. Anufriev, A. Ramiere, K. Termentzidis, D. Lacroix, Phys. Rev. B 95 (20) (2017) 205438.
[35] J. Tang, H.-T. Wang, D.H. Lee, M. Fardy, Z. Huo, T.P. Russell, P. Yang, Nano Lett. 10 (10) (2010) 4279–4283.
[36] J.-K. Yu, S. Mitrovic, D. Tham, J. Varghese, J.R. Heath, Nat. Nanotechnol. 5 (10) (2010) 718–721.
[37] J. Lee, W. Lee, G. Wehmeyer, S. Dhuey, D.L. Olynick, S. Cabrini, C. Dames, J.J. Urban, P. Yang, Nat. Commun. 8 (2017) 14054.

[38] J. Lim, H.-T. Wang, J. Tang, S.C. Andrews, H. So, J. Lee, D.H. Lee, T.P. Russell, P. Yang, ACS Nano 10 (1) (2016) 124–132.

[39] C. Huang, X. Zhao, K. Regner, R. Yang, Phys. E Low-dimens. Syst. Nanostruct. 97 (2018) 277–281.

[40] P.E. Hopkins, L.M. Phinney, P.T. Rakich, R.H. Olsson, I. El-Kady, Appl. Phys. A 103 (3) (2011) 575–579.

[41] P.E. Hopkins, P.T. Rakich, R.H. Olsson, I.F. El-Kady, L.M. Phinney, Appl. Phys. Lett. 95 (16) (2009) 161902.

[42] S. Alaie, D.F. Goettler, M. Su, Z.C. Leseman, C.M. Reinke, I. El-Kady, Nat. Commun. 6 (2015) 7228.

[43] R. Anufriev, J. Maire, M. Nomura, Phys. Rev. B 93 (4) (2016): 045411.

[44] R. Yanagisawa, J. Maire, A. Ramiere, R. Anufriev, M. Nomura, Appl. Phys. Lett. 110 (13) (2017) 133108.

[45] Y.-C. Hua, B.-Y. Cao, J. Phys. Chem. C 121 (9) (2017) 5293–5301.

[46] Q. Hao, G. Chen, M.-S. Jeng, J. Appl. Phys. 106 (11) (2009), 114321/114321-114310.

[47] Q. Hao, D. Xu, H. Zhao, Y. Xiao, F.J. Medina, Sci. Rep. 8 (1) (2018) 9056.

[48] N.K. Ravichandran, A.J. Minnich, Phys. Rev. B 89 (20) (2014) 205432.

[49] Y. He, D. Donadio, J.-H. Lee, J.C. Grossman, G. Galli, ACS Nano 5 (3) (2011) 1839–1844.

[50] B.-Y. Cao, W.-J. Yao, Z.-Q. Ye, Carbon 96 (2016) 711–719.

[51] Q. Hao, G. Chen, M.-S. Jeng, J. Appl. Phys. 106 (11) (2009) 114321.

[52] S. Mazumder, A. Majumdar, J. Heat Transf. 123 (4) (2001) 749–759.

[53] N.K. Ravichandran, H. Zhang, A.J. Minnich, Phys. Rev. X 8 (4) (2018): 041004.

[54] D. Gelda, M.G. Ghossoub, K. Valavala, J. Ma, M.C. Rajagopal, S. Sinha, Phys. Rev. B 97 (4) (2018): 045429.

[55] J.S. Heron, T. Fournier, N. Mingo, O. Bourgeois, Nano Lett. 9 (5) (2009) 1861–1865.

[56] J. Cuffe, E. Chávez, A. Shchepetov, P.-O. Chapuis, E.H. El Boudouti, F. Alzina, T. Kehoe, J. Gomis-Bresco, D. Dudek, Y. Pennec, B. Djafari-Rouhani, M. Prunnila, J. Ahopelto, C.M. Sotomayor Torres, Nano Lett. 12 (7) (2012) 3569–3573.

[57] J.-P.M. Péraud, N.G. Hadjiconstantinou, Phys. Rev. B 84 (20) (2011) 205331.

[58] Q. Hao, G. Zhu, G. Joshi, X. Wang, A. Minnich, Z. Ren, G. Chen, Appl. Phys. Lett. 97 (6) (2010): 063109.

[59] A.J. Minnich, Phys. Rev. Lett. 109 (20) (2012) 205901.

[60] A.N. Tikhonov, V.I. Arsenin, Solutions of Ill-Posted Problems, Winston and Sons, Washington DC, 1977.

[61] A.E. Hoerl, R.W. Kennard, Technometrics 12 (1) (1970) 55–67.

[62] L. Rasmus, DAIMI Report Series 27 (537) (1998).

[63] E. Chavez-Angel, R. Zarate, S. Fuentes, E. Guo, M. Kläui, G. Jakob, New J. Phys. 19 (1) (2017): 013011.

[64] L. Ma, R. Mei, X. Zhao, H. Sun, Semicond. Sci. Technol. 32 (9) (2017): 095008.

[65] M.-Á. Sanchez-Martinez, F. Alzina, J. Oyarzo, C.M. Sotomayor Torres, E. Chavez-Angel, Nanomaterials 9 (3) (2019) 414.

[66] A.A. Maznev, J.A. Johnson, K.A. Nelson, Phys. Rev. B 84 (19) (2011) 195206.

[67] H. Zhang, C. Hua, D. Ding, A.J. Minnich, Sci. Rep. 5 (2014) 9121.

[68] R. Prasher, Nano Lett. 5 (11) (2005) 2155–2159.

[69] K.D. Parrish, J.R. Abel, A. Jain, J.A. Malen, A.J. McGaughey, J. Appl. Phys. 122 (12) (2017) 125101.

[70] A.J. McGaughey, A. Jain, Appl. Phys. Lett. 100 (6) (2012): 061911.

[71] A.M. Marconnet, T. Kodama, M. Asheghi, K.E. Goodson, Nanoscale Microscale Thermophys. Eng. 16 (4) (2012) 199–219.

[72] A. Jain, Y.-J. Yu, A.J.H. McGaughey, Phys. Rev. B 87 (19) (2013) 195301.

[73] G. Romano, J.C. Grossman, J. Heat Transf. 137 (7) (2015): 071302.

[74] G. Romano, A.M. Kolpak, Appl. Phys. Lett. 110 (9) (2017): 093104.

[75] A. Minnich, G. Chen, Appl. Phys. Lett. 91 (7) (2007), 073105-073103.

[76] Q. Hao, H. Zhao, Y. Xiao, D. Xu, J. Appl. Phys. 123 (1) (2018): 014303.

[77] A. Majumdar, J. Heat Transf. 115 (1) (1993) 7–16.

[78] S. Zahiri, J. Zuo, Y. Shen, H. Bao, Appl. Therm. Eng. 141 (2018) 126–133.

[79] Z. Rashid, L. Zhu, W. Li, Phys. Rev. B 97 (7) (2018): 075441.

[80] F. Kargar, B. Debnath, J.-P. Kakko, A. Säynätjoki, H. Lipsanen, D.L. Nika, R.K. Lake, A.A. Balandin, Nat. Commun. 7 (2016) 13400.

[81] A.A. Balandin, D.L. Nika, Mater. Today 15 (6) (2012) 266–275.

[82] M.D. Fischbein, M. Drndić, Appl. Phys. Lett. 93 (11) (2008) 113107.

[83] D. Xu, Q. Wang, X. Wu, J. Zhu, H. Zhao, B. Xiao, X. Wang, X. Wang, Q. Hao, Front. Energy (2018) 1–10.

[84] L. Lindsay, D. Broido, N. Mingo, Phys. Rev. B 82 (11) (2010) 115427.

[85] H. Zhang, C. Hua, D. Ding, A.J. Minnich, Sci. Rep. 5 (2015) 9121.

[86] T. Feng, X. Ruan, Z. Ye, B. Cao, Phys. Rev. B 91 (22) (2015) 224301.